

**Two-pion exchange contributions to the relativistic  $NN$  kernel: Peripheral scattering**

M. D. Cozma

*Institut für Theoretische Physik, Universität Tübingen, Auf der Morgenstelle 14, D-72076 Tübingen, Germany and  
Theory Group, KVI, University of Groningen, Zernikelaan 25, 9747 AA Groningen, The Netherlands*

O. Scholten and R. G. E. Timmermans

*Theory Group, KVI, University of Groningen, Zernikelaan 25, 9747 AA Groningen, The Netherlands*

J. A. Tjon

*Theory Group, KVI, University of Groningen, Zernikelaan 25, 9747 AA Groningen, The Netherlands and  
Department of Physics, National Taiwan University, Taipei 10617, Taiwan*

(Received 17 October 2005; published 19 January 2007)

The relativistic one-boson-exchange model for  $NN$  scattering is extended by including two-pion exchange (TPE) contributions in the kernel. We develop the formalism for the evaluation of the TPE diagrams within the relativistic quasipotential approach. The peripheral partial waves in elastic  $NN$  scattering are studied within this model. The TPE interactions contain a strongly attractive isoscalar-scalar component which requires a low value of the cutoff parameter:  $\Lambda = 650\text{--}800$  MeV. With this prescription, the peripheral waves can be reasonably described.

DOI: [10.1103/PhysRevC.75.014006](https://doi.org/10.1103/PhysRevC.75.014006)

PACS number(s): 21.30.-x, 12.39.Fe, 13.75.Cs

**I. INTRODUCTION**

The one-boson-exchange (OBE) potential model has for many years provided a rather successful and economical description of the nucleon-nucleon ( $NN$ ) interaction. Next to the well-established long-range one-pion-exchange (OPE) force, the model includes the exchanges of heavier mesons, most commonly the  $\eta$ ,  $\rho$ ,  $\omega$ ,  $\delta$  ( $a_0$ ), and  $\sigma$  ( $f_0$ , or  $\epsilon$ ). The OBE model naturally leads to a medium-range attraction, a strong spin-orbit force, and short-range repulsion. With a limited number of free parameters, it can provide a very reasonable fit to the  $NN$  scattering data [1,2]. A Lorentz covariant OBE model was developed in Ref. [3] by solving the Bethe-Salpeter equation for the  $NN$  system in the equal-time approximation. This relativistic model has been applied to pion production in  $NN$  scattering [4], to electron scattering on the deuteron [5], and to proton-proton bremsstrahlung [6,7].

One of the reasons why OBE models became popular in the 1960s was the failure, dating back to the 1950s, to formulate consistently and successfully the two-pion exchange (TPE) interaction in field theory. It was not known how to properly regularize and renormalize the TPE diagrams or, in fact, which TPE interactions to include. Therefore, the ambitions to derive at least the long- and medium-range  $NN$  interaction from field theory were mostly dropped in the 1960s. (The connection of the OBE model to QCD, on the other hand, is tenuous at best [8].) It is now understood that the key to the solution is chiral symmetry within the concept of an effective field theory (EFT). During the last 15 years or so, the ambitions of the 1950s have been picked up and attempts have been made to formulate a (nonrelativistic) EFT, in terms of nucleon and pion degrees of freedom, that obeys the constraints of spontaneously broken chiral symmetry as it is present in QCD [9–13]. This has proven to be far from straightforward, and, at present, there are still open questions about the power counting that

ranks the various short- and long-range terms in the hierarchy of interactions in the EFT [14]. Nevertheless, a rather good description of the  $NN$  phase shifts has been obtained in this approach [11,15,16]. Also, the TPE interaction derived from this chiral EFT [10,17–19], when added to OPE, provides a high-quality long-range  $NN$  interaction [19,20].

In this paper, we want to extend the kernel of the relativistic OBE model of Ref. [3] by including one-loop TPE diagrams. Our choice for the TPE interaction is motivated by the effective chiral Lagrangian used in nonrelativistic EFT; however, we lack the power counting that makes the nonrelativistic EFT approach, in principle, systematically improvable. Our goal is to investigate whether with the addition of such TPE diagrams to the relativistic kernel, a good description of the phase shifts is possible and to study the effect of relativistic corrections and recoil terms that are naturally included in a Lorentz covariant framework. Such an  $NN$  model with TPE would find many applications in the relativistic few-body problem. To this aim, we will first develop the necessary formalism for a relativistic treatment of TPE, and then we will apply this formalism to elastic  $NN$  scattering. We will restrict ourselves in this paper to  $D$  and higher waves, which we will attempt to describe by OPE and TPE only, leaving out the short-range heavy-boson exchange interactions.

Our paper is organized as follows. In Sec. II we describe briefly the relativistic quasipotential approximation to elastic  $NN$  scattering, in particular the BSLT equation. In Sec. III we discuss the TPE additions to the OBE kernel. The evaluation of the one-loop diagrams is discussed in detail. Section IV is dedicated to the presentation of our main results, the predictions for the values of the phase shifts for the peripheral waves up to 300 MeV laboratory energy, obtained in perturbation theory and by iteration of the quasipotential. The numerical accuracy of our results is also addressed. We end with a summary and final conclusions in Sec. V.

## II. QUASIPOTENTIAL APPROACH TO $NN$ SCATTERING

In relativistic field theories, the  $T$  matrix for scattering of two nucleons is a solution of the inhomogeneous Bethe-Salpeter (BS) equation

$$T(p, p'; P) = V(p, p') - i \int \frac{d^4k}{(2\pi)^4} V(p, k) G_2(k, P) T(k, p'; P), \quad (1)$$

where  $G_2(p, P)$  is the two-body propagator given by the direct product of two one-particle free-fermion propagators with relative momentum  $p$  and total momentum  $P$ . In principle, the kernel  $V$  has to be taken as the sum of all irreducible diagrams. This is clearly an impossible task, and therefore one usually resorts to a quasipotential approximation. The full BS equation, written now in symbolic form,

$$T = V + V S T, \quad (2)$$

is replaced by a set of two coupled equations,

$$T = W + W g T, \quad (3)$$

$$W = V + V (G - g) W, \quad (4)$$

which are equivalent with the original BS equation, as depicted graphically in Fig. 1. The new propagator  $g$  is chosen by restricting the relative energy in some way, while preserving properties such as two-particle unitarity and relativistic covariance. Of several possibilities [21], we will adopt the so-called Blankenbecler-Sugar-Logunov-Tavkhelidze [22] (BSLT) approximation. The BSLT equation has been applied successfully to the coupled  $NN$ - $N\Delta$  scattering problem [4], to electron-deuteron scattering [5], and to proton-proton bremsstrahlung [6,7]. It consists of replacing the scalar part of the two-nucleon propagator

$$G_0 = \frac{1}{(\frac{1}{2}P + p)^2 - M^2 + i\epsilon} \frac{1}{(\frac{1}{2}P - p)^2 - M^2 + i\epsilon} \quad (5)$$

by

$$G_2^{\text{BSLT}} = i\pi \frac{1}{E_p - E} \frac{1}{(E_p + E)^2} \delta(p_0), \quad (6)$$

where  $M$  is the nucleon mass. The two-particle propagator becomes

$$G_2^{\text{BSLT}}(p, P) = \frac{1}{2}(E_p - E)\delta(p_0)S^{(1)}(p, P)S^{(2)}(-p, P), \quad (7)$$

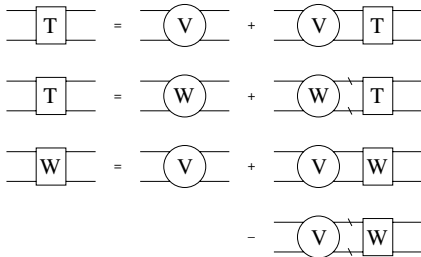


FIG. 1. Graphical representation of the BS equation (first line), BSLT equation (second line), and integral equation satisfied by the quasipotential (third line). Quasipotential propagator  $g$  is denoted by a crossed line.

where  $E = \frac{1}{2}P_0$  and  $E_p = \sqrt{p^2 + M^2}$ ;  $S^{(1)}(p, P)$  and  $S^{(2)}(-p, P)$  denote the Dirac propagators of the nucleon labeled by 1 and 2, respectively. By using this form of the propagator, the integration over the relative energy can be performed in the BS equation. One is then left with the BSLT equation, which can be handled more easily from a practical point of view,

$$T(\hat{p}, \hat{p}'; P) = W(\hat{p}, \hat{p}') - i \int \frac{d^4k}{(2\pi)^4} W(\hat{p}, \hat{k}) G_2^{\text{BSLT}}(\hat{k}, P) T(\hat{k}, \hat{p}'; P), \quad (8)$$

where the four-momentum  $\hat{k}$  is restricted by the  $\delta$  function in  $S_2$  such that in the center-of-mass frame of the two nucleons its time component is zero, i.e.,  $\hat{k}_0 = 0$ .

The kernel  $W$  of the BSLT equation, the so-called quasipotential, can be determined from Eq. (4), which is represented graphically in the third line of Fig. 1. In previous works, the potential  $V$  was taken as the sum of tree-level OBE diagrams. Our goal in this paper is to extend the kernel by also including next to the OBE diagrams the one-loop irreducible diagrams, i.e., the TPE interaction, in the potential  $V$ .

## III. TWO-PION EXCHANGE INTERACTION

### A. The chiral Lagrangian and two-pion exchange

The derivation of the TPE interaction proceeds from the chiral Lagrangian density constructed in terms of covariant derivatives for the pion and the nucleon field [23]:

$$\vec{D}^\mu = D^{-1} \partial^\mu \vec{\pi} / F_\pi = \frac{1}{1 + \vec{\pi}^2 / F_\pi^2} \partial^\mu \vec{\pi} / F_\pi, \quad (9)$$

$$D^\mu \psi = (\partial^\mu + \vec{\tau} \cdot \vec{E}^\mu) \psi = \left( \partial^\mu + \frac{i}{F_\pi} c_0 \vec{\tau} \cdot \vec{\pi} \times \vec{D}^\mu \right) \psi, \quad (10)$$

where  $F_\pi = 185$  MeV is the pion decay constant, and  $g_A = 1.26$  is the Gamow-Teller coupling in neutron  $\beta$  decay;  $\tau_i$  are the Pauli isospin matrices. For convenience later on, we have added the coupling constant  $c_0$  in front of the Weinberg-Tomozawa (WT)  $NN2\pi$  seagull interaction; chiral symmetry requires that  $c_0 \equiv 1$ . With these chiral-covariant derivatives as building blocks, the chiral Lagrangian can be constructed as a sum of terms with an increasing number of such derivatives. The presence of the nucleon as a heavy degree of freedom in this Lorentz covariant chiral Lagrangian spoils the one-to-one correspondence between loop and momentum expansion as it exists in chiral perturbation theory in the meson sector [24]. A consistent chiral power counting scheme can be obtained, however, with the heavy-baryon formalism, which implies that the nonrelativistic limit has to be taken for the nucleon [9,25,26].

The Lagrangian densities relevant for OPE and TPE are given by

$$\mathcal{L}^{(0)} = \bar{\psi} \left( i \gamma_\mu \partial^\mu - M - \frac{c_0}{F_\pi^2} \gamma_\mu \vec{\tau} \cdot \vec{\pi} \times \partial^\mu \vec{\pi} + \frac{g_A}{F_\pi} \gamma_\mu \gamma_5 \vec{\tau} \cdot \partial^\mu \vec{\pi} \right) \psi, \quad (11)$$

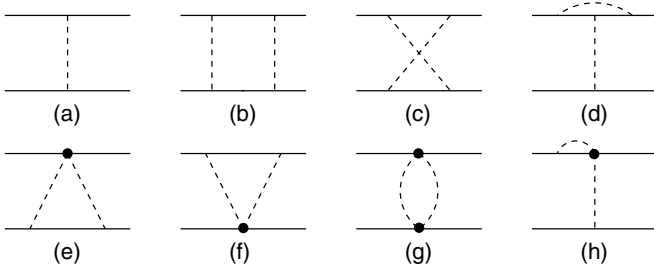


FIG. 2. Tree-level and one-loop diagrams contributing to the OPE and TPE potentials. The  $NN2\pi$  WT vertex is represented by a full circle.

$$\begin{aligned} \mathcal{L}^{(1)} = & -\frac{8c_1}{F_\pi^2} m_\pi^2 \bar{\psi} \psi \bar{\pi}^2 - \frac{2c_2}{M^2 F_\pi^2} (\bar{\psi} \partial_\mu \partial_\nu \psi \partial^\mu \bar{\pi} \cdot \partial^\nu \bar{\pi} + \text{h.c.}) \\ & + \frac{4c_3}{F_\pi^2} \bar{\psi} \psi \partial_\mu \bar{\pi} \cdot \partial^\mu \bar{\pi} - \frac{2c_4}{F_\pi^2} (\bar{\psi} \sigma_{\mu\nu} \bar{\tau} \psi) \cdot \partial^\mu \bar{\pi} \times \partial^\nu \bar{\pi}. \end{aligned} \quad (12)$$

The dimensionful coupling constants (also called “low-energy constants”)  $c_1$ ,  $c_2$ ,  $c_3$ , and  $c_4$  of the  $NN2\pi$  seagull terms in the Lagrangian density are defined according to the convention used in chiral perturbation theory. Their values have been extracted from fits to pion-nucleon amplitudes [27,28] and  $NN$  scattering data [19,20]. For our numerical results, we will adopt the values  $c_1 = -0.81$ ,  $c_2 = 3.28$ ,  $c_3 = -4.70$ , and  $c_4 = +3.40 \text{ GeV}^{-1}$ . The sensitivity of the phase shifts to variations in the coupling constants is discussed below.

A systematic expansion of the Lagrangian densities in Eqs. (11) and (12) to order  $1/M$  gives the chiral Lagrangian density used in chiral EFT of  $NN$  scattering [9,10]. The relevant diagrams are given in Figs. 2 and 3. Tree-level OPE is depicted in Fig. 2(a). Figures 2(b)–2(h) show the leading TPE diagrams. The direct-box diagram, Fig. 2(b), is reducible, and part of it is generated by iterating the BSLT equation with OPE. The diagrams in Figs. 2(d) and 2(h) represent vertex corrections to the OPE potential [29]. Subleading TPE contributions are given in Fig. 3. They are triangle graphs with one  $NN2\pi$  vertex with the coupling constant  $c_{1..4}$ , and “football” graphs with one WT vertex and one subleading  $NN2\pi$  interaction. We include here the relativistic counterparts of all these TPE diagrams. As pointed out above, we lack the systematic framework of nonrelativistic EFT. Our

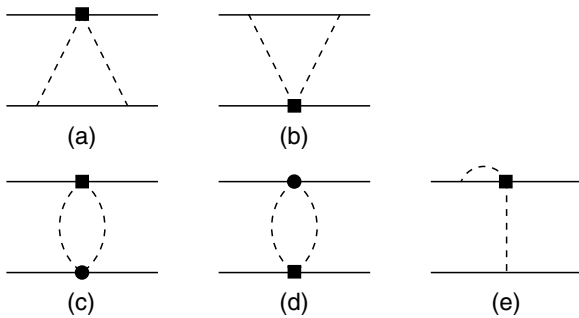


FIG. 3. One-loop diagrams contributing to TPE potential. WT interaction is represented by a full circle, and  $NN2\pi$  vertices with coupling constants  $c_1$ ,  $c_3$ , or  $c_4$  by a full square.

main goal is to see if within the quasipotential approach a good description of  $NN$  scattering can be obtained with a long-range interaction of OPE and TPE. For convenience, we will still refer to the diagrams as belonging to next-to-leading order (NLO, leading) and next-to-next-to-leading order (NNLO, subleading) TPE in the following, keeping in mind that this terminology belongs to the corresponding diagrams in nonrelativistic EFT.

The diagrams in Figs. 2(d), 2(h), and 3(e) represent vertex corrections to OPE. In chiral EFT, the vertex corrections to OPE and self-energies contribute to this order only to mass and coupling constant renormalization [17]. In a relativistic calculation with pseudoscalar pion-nucleon interaction, such contributions were found by Wortman [30] to be of the order of 10% of the direct- and crossed-box contributions, with similar expectations for the pseudovector case. We do not evaluate any of the vertex and self-energy diagrams explicitly in this paper, their contributions being effectively taken into account by using the physical values for masses and coupling constants.

The resulting TPE potentials contain isospin-dependent central, spin-spin, tensor, and spin-orbit terms. In Fig. 4, we plot as an example the isospin-independent scalar potential and the isospin-dependent tensor potential in comparison with the corresponding OBE potentials [5]. The former contains a very strong attractive contribution from the triangle diagram with a  $c_3$  vertex, and the latter a strong contribution from the triangle diagram with a  $c_4$  vertex. The TPE potentials displayed in Fig. 4 were obtained by Kaiser [17,31] in chiral perturbation theory up to  $N^3\text{LO}$  using dimensional regularization to render the loop integrals finite. The apparent difference between the chiral TPE and OBE potentials at short range can be “cured” by using a different regularization procedure for the TPE loop integrals, i.e., by introducing a cutoff that ensures that high momentum contributions are left out [32]. The nonrelativistic TPE potentials are discussed in more detail in Refs. [17–19].

## B. Irreducible TPE diagrams

The quasipotential  $W$  is determined as the sum of all irreducible two-particle diagrams plus the sum of their iteration, as symbolically presented in Eq. (4). In this section, we will present the explicit expressions of the one-loop contributions to  $W$ : the one-loop TPE contributions and the iterated OPE diagram. They represent, as discussed already in the previous section, the truncation of the full  $W$  kernel. The labeling convention used for the momenta associated with a generic one-loop diagram is exemplified in Fig. 5 for the direct-box diagram. To make our normalization convention clear and to facilitate comparison with other similar works, we begin by listing the amplitude for the OPE diagram [the connection with the partial-wave  $T$  matrix in Eq. (38) is an extra factor,  $i\pi$ ], that is,

$$\begin{aligned} I^{(\text{OPE})} = & \alpha^{(\text{OPE})} \frac{[\bar{u}(q_1) \not{k} \gamma_5 u(p_1)]^{(1)} \times [\bar{u}(q_2) \not{k} \gamma_5 u(p_2)]^{(2)}}{k^2 - m_\pi^2}, \\ \alpha^{(\text{OPE})} = & -\frac{i}{\pi} \frac{g_A^2}{4\pi F_\pi^2} [2I(I+1) - 3]. \end{aligned} \quad (13)$$

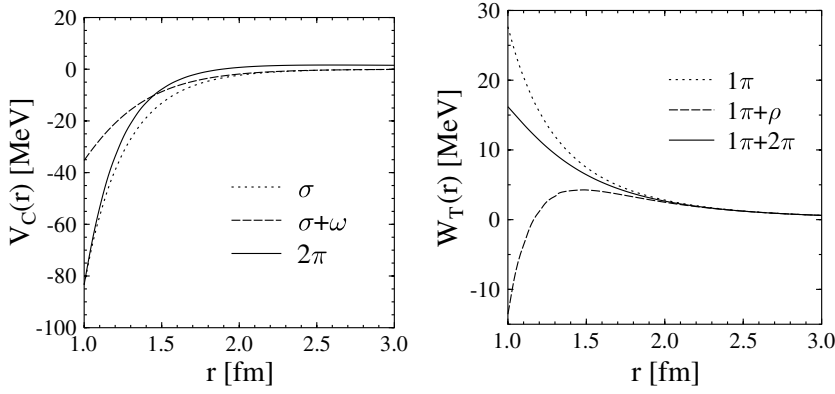


FIG. 4. Isospin-independent central potential  $V_C(r)$  (a) and the isospin-dependent tensor potential  $W_T(r)$  (b) generated by the TPE diagrams compared with the corresponding OBE potentials.

The direct- and crossed-box diagrams are given, respectively, by

$$I^{(\text{DB})} = \alpha^{(\text{DB})} \int d^4k \frac{[\bar{u}(q_1)(\not{k} + \not{p}_1 - \not{q}_1) \gamma_5 (\not{k} + \not{p}_1 + M) \not{k} \gamma_5 u(p_1)]^{(1)}}{(k + p_1)^2 - M^2} \times \frac{[\bar{u}(q_2)(\not{k} + \not{q}_2 - \not{p}_2) \gamma_5 (\not{p}_2 - \not{k} + M) \not{k} \gamma_5 u(p_2)]^{(2)}}{(k - p_2)^2 - M^2} D_{\pi_1\pi_2}, \quad (14)$$

and

$$I^{(\text{CB})} = \alpha^{(\text{CB})} \int d^4k \frac{[\bar{u}(q_1)(\not{k} + \not{p}_1 - \not{q}_1) \gamma_5 (\not{k} + \not{p}_1 + M) \not{k} \gamma_5 u(p_1)]^{(1)}}{(k + p_1)^2 - M^2} \times \frac{[\bar{u}(q_2) \not{k} \gamma_5 (\not{k} + \not{q}_2 + M) (\not{k} + \not{p}_1 - \not{q}_1) \gamma_5 u(p_2)]^{(2)}}{(k + q_2)^2 - M^2} D_{\pi_1\pi_2}. \quad (15)$$

The coefficients  $\alpha^{(\text{DB})}$  and  $\alpha^{(\text{CB})}$  contain coupling constants and normalization and isospin factors. For the direct- and crossed-box diagrams, they read

$$\alpha^{(\text{DB})} = \frac{1}{4\pi^4} \left( \frac{g_A^2}{4\pi F_\pi^2} \right)^2 [9 - 4I(I + 1)], \quad (16)$$

$$\alpha^{(\text{CB})} = \frac{1}{4\pi^4} \left( \frac{g_A^2}{4\pi F_\pi^2} \right)^2 [4I(I + 1) - 3],$$

where  $I$  is the total isospin of the two-nucleon system. The pion-nucleon coupling constant is here  $g_A/F_\pi$ , which can be

related to the physical coupling constant by the Goldberger-Treiman relation  $g_A/F_\pi = \sqrt{4\pi} f/m_\pi$ , where  $f^2 \simeq 0.075$  and  $m_\pi$  is used as scaling mass to make  $f$  dimensionless [33]. The pion propagators are included in the factor  $D_{\pi_1\pi_2}$  given by

$$D_{\pi_1\pi_2} = \frac{1}{k^2 - m_\pi^2} \frac{1}{(k + p_1 - q_1)^2 - m_\pi^2}. \quad (17)$$

The expression for the triangle diagram with the WT vertex in Fig. 2(e) is given by

$$I^{(\text{TR}_{c_0})} = \alpha^{(\text{TR}_{c_0})} \int d^4k \frac{[\bar{u}(q_1)(\not{k} + \not{p}_1 - \not{q}_1) \gamma_5 (\not{k} + \not{p}_1 + M) \not{k} \gamma_5 u(p_1)]^{(1)}}{(k + p_1)^2 - M^2} \times [\bar{u}(q_2)(2\not{k} + \not{p}_1 - \not{q}_1) u(p_2)]^{(2)} D_{\pi_1\pi_2}. \quad (18)$$

The expression for the other triangle diagram can be obtained by replacing  $p_1$  and  $q_1$  with  $p_2$  and  $q_2$ , respectively, and changing the sign of the integration variable  $k$ . The expression for the football diagram with two WT

vertices is

$$I^{(\text{FT}_{c_0})} = \alpha^{(\text{FT}_{c_0})} \int d^4k [\bar{u}(q_1)(2\not{k} + \not{p}_1 - \not{q}_1) u(p_1)]^{(1)} \times [\bar{u}(q_2)(2\not{k} - \not{p}_2 + \not{q}_2) u(p_2)]^{(2)} D_{\pi_1\pi_2}. \quad (19)$$

For these diagrams, the coefficients  $\alpha$  are given, respectively, by

$$\alpha^{(\text{TR}_{c_0})} = -\frac{1}{16\pi^5} \frac{c_0}{F_\pi^2} \frac{g_A^2}{4\pi F_\pi^2} [4I(I+1) - 6], \quad (20)$$

$$\alpha^{(\text{FT}_{c_0})} = \frac{1}{2} \frac{1}{(2\pi)^6} \left( \frac{c_0}{F_\pi^2} \right)^2 [4I(I+1) - 6].$$

The triangle diagrams of Fig. 3(a) are given by

$$I^{(\text{TR}_{c_i})} = \alpha^{(\text{TR}_{c_i})} \int d^4k \frac{[\bar{u}(q_1)(\not{k} + \not{p}_1 - \not{q}_1) \gamma_5 (\not{k} + \not{p}_1 + M) \not{k} \gamma_5 u(p_1)]^{(1)}}{(k+p_1)^2 - M^2} \times [\bar{u}(q_2) O_i u(p_2)]^{(2)} D_{\pi_1\pi_2}, \quad (21)$$

with  $i = 1, 3, 4$ . The corresponding operators  $O_i$  are

$$\begin{aligned} O_1 &= 1, \\ O_2 &= 2[(k \cdot p_2)(k + q_2 - p_2) \cdot p_2 \\ &\quad + (k \cdot q_2)(k + q_2 - p_2) \cdot q_2], \\ O_3 &= k \cdot (k - p_2 + q_2), \\ O_4 &= (p_2 - q_2) \not{k} - \not{k} (p_2 - q_2), \end{aligned} \quad (22)$$

and the coefficients are given by

$$\begin{aligned} \alpha^{(\text{TR}_{c_1})} &= \frac{3}{\pi^5} \frac{g_A^2}{4\pi F_\pi^2} \frac{c_1 m_\pi^2}{F_\pi^2}, \\ \alpha^{(\text{TR}_{c_2})} &= -\frac{3}{8\pi^5} \frac{g_A^2}{4\pi F_\pi^2} \frac{c_2}{M^2 F_\pi^2}, \\ \alpha^{(\text{TR}_{c_3})} &= -\frac{3}{2\pi^5} \frac{g_A^2}{4\pi F_\pi^2} \frac{c_3}{F_\pi^2}, \\ \alpha^{(\text{TR}_{c_4})} &= -\frac{1}{8\pi^5} \frac{g_A^2}{4\pi F_\pi^2} \frac{c_4}{F_\pi^2} [4I(I+1) - 6]. \end{aligned} \quad (23)$$

The expression of the triangle diagrams of Fig. 3(b) can be obtained from these formulas by a permutation of the variables referring to nucleons 1 and 2.

Of the football diagrams with one WT vertex and one  $c_i$  ( $i = 1, 3, 4$ ) vertex, only the  $c_0 c_4$  football diagram will give a finite contribution, viz.,

$$I^{(\text{FT}_{c_0 c_4})} = \alpha^{(\text{FT}_{c_0 c_4})} \int d^4k [\bar{u}(q_1) (2\not{k} + \not{p}_1 - \not{q}_1) u(p_1)]^{(1)} \times [\bar{u}(q_2) ((\not{p}_2 - \not{q}_2) \not{k} - \not{k} (\not{p}_2 - \not{q}_2)) u(p_2)]^{(2)} D_{\pi_1\pi_2}, \quad (24)$$

with

$$\alpha^{(\text{FT}_{c_0 c_4})} = -\frac{1}{(2\pi)^6} \frac{c_0 c_4}{F_\pi^4} [4I(I+1) - 6]. \quad (25)$$

In the above expressions, all the meson-nucleon vertices were considered to be pointlike. In the actual calculations, pointlike (dimensional regularization calculation) and dipole form factor (cutoff regularization calculation) type vertices

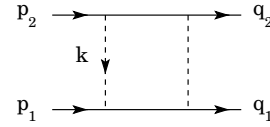


FIG. 5. Labeling momenta for the direct-box diagram. Integration momentum  $k$  is always assigned to the meson line attached to the incoming nucleon 1.

were used alternatively. In the latter case, a dipole form factor that depended on the momentum of the exchanged meson was taken into account at each vertex. To arrive at the corresponding expressions for the loop integrals, one has to make the following substitution for the pion propagator:

$$\frac{1}{k^2 - m_\pi^2} \rightarrow \frac{1}{k^2 - m_\pi^2} \left( \frac{\Lambda^2}{k^2 - \Lambda^2} \right)^2. \quad (26)$$

### C. The quasipotential direct box

The quasipotential direct box can be obtained by substituting in the expression of the full direct box, Eq. (14), the scalar part of the intermediate two-fermion propagator with its BSLT version as given in Eq. (6). The  $k_0$  integral can then be trivially performed. In principle, at this stage a simple three-dimensional numerical integration will provide the final answer (after properly taking care of the principal-value singularities), but a decomposition of the remaining integral in small pieces will allow us to implement a numerical dimensional regularization besides the cutoff one. We use here a different labeling convention, more appropriate for the direct-box diagram, for the integration four-momentum  $k$ , cf. Fig. 6. The first step is the decomposition of the operators

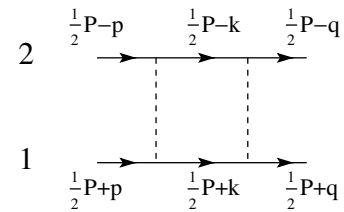


FIG. 6. Labeling convention used for computation of quasipotential direct box.  $P = (2E, \vec{0})$  is the total momentum in the c.m. frame, and  $p, q, k$  are relative momenta. Quasipotential approximation implies  $k_0 = 0$ , while for the other two momenta similar relations hold only on-shell.

belonging to each of the two fermion lines into monomials of  $k = |\vec{k}|$ , the length of the integration three-momentum  $\vec{k}$ . (We will limit ourselves to the on-shell case here. A generalization to the half-off-shell case needed for the iteration of the BSLT equation is straightforward.) For fermion line 1, see Fig. 6, one has

$$\begin{aligned} O_1 &= \sum_{i=0,3} O_1^i k^i, \\ O_1^0 &= (E^3 + 3ME)\gamma_0 - (M^3 + 3ME^2), \\ O_1^1 &= -(E^2 + 3M^2)\vec{\gamma} \cdot \hat{k}, \\ O_1^2 &= -E\gamma_0 + 3M, \\ O_1^3 &= \vec{\gamma} \cdot \hat{k}. \end{aligned} \quad (27)$$

Fermion line 2 is identical to fermion line 1 except for a minus sign in front of each appearance of  $\vec{k}$ , i.e.,

$$\begin{aligned} O_2 &= \sum_{i=0,3} O_2^i k^i, \\ O_2^i &= (-1)^i O_1^i. \end{aligned} \quad (28)$$

The expression of the quasipotential direct box can then be written as

$$\begin{aligned} I^{(\text{QDB})} &= \alpha^{(\text{DB})} \sum_{i,j=0}^3 \int d\Omega_{\vec{k}} \left[ \bar{u} \left( \frac{1}{2}P + q \right) O_1^i u \left( \frac{1}{2}P + p \right) \right] \\ &\quad \times \left[ \bar{u} \left( \frac{1}{2}P - q \right) O_2^j u \left( \frac{1}{2}P - p \right) \right] \cdot I(d, i + j), \end{aligned} \quad (29)$$

$$I(d, l) = -\frac{1}{2} \int_0^\infty dk \frac{k^{d+l-1}}{(E + E_{\vec{k}})^2 (E - E_{\vec{k}})} \frac{1}{(\vec{k} - \vec{q})^2 + m_\pi^2} \frac{1}{(\vec{k} - \vec{p})^2 + m_\pi^2}, \quad (30)$$

where the symbol  $d$  represents the number of spatial dimensions. Divergences can only occur from the one-dimensional integral  $I(d, l)$ . It can be regulated with a form factor of dipole type, or via dimensional regularization. In the latter case, the divergent integrals have to be decomposed further, in order to isolate the ultraviolet divergence from the principal-value pole. With specific techniques, the integrals can then be evaluated and the infinities removed analytically. A simpler method is to subtract from the divergent integrands their asymptotic form (with sufficient terms in the asymptotic expansion) to render finite integrals that can be evaluated numerically. The asymptotic integrands are of a Laurent series type, and the respective integrals can easily be evaluated and dimensionally regularized. This second method has been used in the actual calculations.

#### D. Evaluation of one-loop integrals

The evaluation of the relativistic TPE diagrams in this work is based on the general method for evaluating one-loop integrals invented by Passarino and Veltman [34,35]. The method has already been applied to the case of relativistic  $NN$  scattering by Zuilhof and Tjon [36] to evaluate the direct- and crossed-box TPE diagrams with both pseudoscalar and pseudovector coupling. We follow closely the procedure described in Ref. [36]; for completeness, the relevant steps are reproduced here. (Similar techniques have been applied by Celenza *et al.* [37].) We define the scalar and tensor two-, three-, and four-point functions by [34]

$$\begin{aligned} B_0; B_\mu; B_{\mu\nu} &= \int d^4k \frac{1; k_\mu; k_\mu k_\nu}{[k^2 - m_1^2] [(k+p)^2 - m_2^2]}, \\ C_0; C_\mu; C_{\mu\nu}; C_{\mu\nu\rho} &= \int d^4k \frac{1; k_\mu; k_\mu k_\nu; k_\mu k_\nu k_\rho}{[k^2 - m_1^2] [(k+p)^2 - m_2^2] [(k+p+q)^2 - m_3^2]}, \\ D_0; D_\mu; D_{\mu\nu}; D_{\mu\nu\rho} &= \int d^4k \frac{1; k_\mu; k_\mu k_\nu; k_\mu k_\nu k_\rho}{[k^2 - m_1^2] [(k+p)^2 - m_2^2]} \\ &\quad \times \frac{1}{[(k+p+q)^2 - m_3^2] [(k+p+q+r)^2 - m_4^2]}. \end{aligned} \quad (31)$$

The scalar  $n$ -point functions  $B_0, C_0$ , and  $D_0$  have to be evaluated explicitly, either numerically or, where possible, by using the analytic expressions. The tensor  $n$ -point functions can be written in terms of scalar moments, which in turn can be

evaluated in terms of lower rank moments and/or scalar point functions. Some details about this reduction and nomenclature are given in the Appendix. The complete set of formulas can be found in Ref. [34]. The convention for labeling the

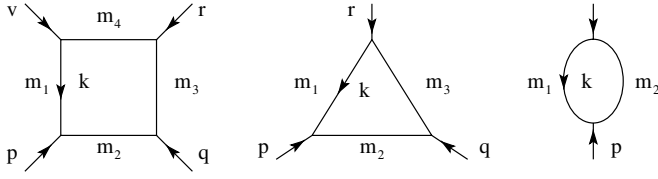


FIG. 7. Conventions used for labeling the four momenta for the four-, three-, and two-scalar functions, respectively, from left to right.

external momenta and internal masses is shown in Fig. 7 and agrees with the convention used in Ref. [34]. For our purposes, tensor  $n$ -point functions up to  $D_{\mu\nu}$  and  $C_{\mu\nu\rho}$  were needed. They were computed by using the *ff* package developed by van Oldenborgh and Vermaseren [38,39] in terms of the scalar moments for the two-, three-, and four-point functions (introduced in the Appendix).

A one-loop diagram with at most four external legs can be written as

$$L = \sum_{r=0}^{N_B} O_B^{\mu_1 \dots \mu_r} [r] B_{\mu_1 \dots \mu_r} + \sum_{r=0}^{N_C} O_C^{\mu_1 \dots \mu_r} [r] C_{\mu_1 \dots \mu_r} + \sum_{r=0}^{N_D} O_D^{\mu_1 \dots \mu_r} [r] D_{\mu_1 \dots \mu_r}, \quad (32)$$

by separating the  $k_{\mu_1} \dots k_{\mu_r}$  term from the spinor part of the numerator and then, together with the scalar parts of the internal propagators, identifying them with the scalar and tensor loop integrals in Eq. (31). Here  $N_B$ ,  $N_C$ , and  $N_D$  are the highest ranks appearing for the given diagram for the tensor two-, three-, and four-point functions, respectively. By making use of the expression of the tensor loop integrals in terms of scalar moments (see the Appendix), the expression of the one-loop diagram reads

$$L = \sum_{r=0}^{N_B} \sum_{i=1}^{n_r^B} O_B[r, i] B_{ri} + \sum_{r=0}^{N_C} \sum_{i=1}^{n_r^C} O_C[r, i] C_{ri} + \sum_{r=0}^{N_D} \sum_{i=1}^{n_r^D} O_D[r, i] D_{ri}. \quad (33)$$

The coefficients  $n_r^B$ ,  $n_r^C$ , and  $n_r^D$  represent for a given  $r$  the number of moments  $B_r$ ,  $C_r$ , and  $D_r$ . For example,  $n_1^C = 2$  and  $n_2^C = 4$ , as can be seen from Eq. (A2). The operators  $O_B$ ,  $O_C$ , and  $O_D$  contain the complete spin structure of the diagram in question, and for the case of two-fermion scattering can be put in the form

$$O_M[r, i] = O_M^{(1)}[r, i] \times O_M^{(2)}[r, i], \quad M = B, C, D, \quad (34)$$

with the superscripts denoting the fermion line number. Their matrix elements between the two-particle helicity states are then evaluated in the center-of-mass frame of the two nucleons. The two-particle states are the direct product of one-particle

helicity spinors which satisfy the Dirac equation

$$\not{p} u_{\Lambda}^{\pm}(\vec{p}) = [M + \gamma^0 (p_0 \mp E_p)] u_{\Lambda}^{\pm}(\vec{p}), \quad (35)$$

$$p = (p_0, \vec{p}), \quad E_p = \sqrt{M^2 + \vec{p}^2},$$

where the upper index  $\pm$  labels the positive- or negative-energy solutions. In the two-fermion spin space, the following 16 operators form a basis [36]:

$$\begin{aligned} O_1 &= 1^{(1)} 1^{(2)}, & O_2 &= \gamma_0^{(1)} 1^{(2)}, & O_3 &= 1^{(1)} \gamma_0^{(2)}, \\ O_4 &= \gamma_0^{(1)} \gamma_0^{(2)}, & O_5 &= \gamma_{\mu}^{(1)} \gamma^{\mu(2)}, & O_6 &= \gamma_0^{(1)} O_5, \\ O_7 &= O_5 \gamma_0^{(2)}, & O_8 &= \gamma_0^{(1)} O_5 \gamma_0^{(2)}, & O_9 &= \gamma_5^{(1)} \gamma_5^{(2)}, \\ O_{10} &= \gamma_0^{(1)} O_9, & O_{11} &= O_9 \gamma_0^{(2)}, & O_{12} &= \gamma_0^{(1)} O_9 \gamma_0^{(2)}, \\ O_{13} &= \gamma_5^{(1)} O_5 \gamma_5^{(2)}, & O_{14} &= \sigma_{\mu\nu}^{(1)} \sigma^{\mu\nu(2)}, & O_{15} &= \gamma_0^{(1)} O_{14}, \\ O_{16} &= O_{14} \gamma^{(2)}. \end{aligned}$$

By applying the off-shell Dirac equation (35), the spin structure can be readily reduced to a linear combination of these operators, that is, one can write

$$O_M[r, i] = \sum_{j=1}^{16} b_j^M[r, j] O_j, \quad M = B, C, D, \quad (36)$$

which leads to the final expression for a specific diagram:

$$L = \sum_{j=1}^{16} c_j O_j, \quad c_j = \sum_{r=0}^{N_B} \sum_{i=1}^{n_r^B} b_j^B[r, i] B_{ri} + \sum_{r=0}^{N_C} \sum_{i=1}^{n_r^C} b_j^C[r, i] C_{ri} + \sum_{r=0}^{N_D} \sum_{i=1}^{n_r^D} b_j^D[r, i] D_{ri}. \quad (37)$$

The evaluation of the  $c_j$  coefficients involves cumbersome algebraic operations, and because of the large number of terms, an automated evaluation of these coefficients was desirable. For this purpose, the computer algebra program FORM [40] was used to write a code that determines the analytical expression for each of the  $c_j$  for a particular diagram in terms of the scalar moments and of the kinematic variables of the process. Next, the values of the scalar moments were computed using the *ff* package, which in turn allowed the numerical evaluation of the coefficients  $c_j$ . Then the matrix elements of the sixteen  $O_j$  operators in the two-particle helicity basis were computed, and by using Eq. (37) the numerical value of the one-loop diagram was obtained. For the chosen Lagrangian density, only the coefficients  $c_1, \dots, c_8$  are nonzero. An example of the scheme outlined in this section can be found in Ref. [36], where the expression of the coefficients  $c_j$  is determined step-by-step for the crossed-box TPE diagram with pseudoscalar pion-nucleon interaction.

Finally, the BSLT equation was solved in a partial-wave basis. This implies that one has to determine from the general helicity amplitudes, the determination of which was outlined in this section, the values of the partial-wave amplitudes

$T_J^J$  (singlet or uncoupled triplet),  $T_{J\pm 1}^J$  (diagonal coupled-triplet amplitudes), and  $T_{J,J\pm 1}^J$  (off-diagonal coupled-triplet amplitudes). This was achieved by employing the partial-wave projection formalism of Kubis [41].

## IV. RESULTS AND DISCUSSION

### A. Peripheral waves

In this paper, we will apply the formalism developed in the previous sections to the ‘‘peripheral’’ partial waves in  $NN$  scattering, more specifically, to  $D$ ,  $F$ , and  $G$  waves. In nonrelativistic chiral EFT with Weinberg power counting, there are no zero-range counterterms present in these waves in NNLO, only OPE and leading and subleading TPE. We will investigate here to what extent we can describe these waves with only OPE and TPE in a relativistic framework, by comparing our results with the phase shifts and mixing angles from the energy-dependent partial-wave analysis PWA93 [42]. In a followup work, we will then investigate the lower partial waves.

At NNLO in chiral EFT, using dimensional regularization to extract the finite part of the one-loop TPE integrals, the peripheral waves for  $NN$  scattering are reasonably reproduced up to about 50 MeV for the  $D$  waves and up to about 150 MeV for the higher partial waves [17]. The convergence of the chiral expansion suffers from the short-range behavior of the NNLO TPE diagrams, in particular because of the very strong central attraction resulting from the triangle diagrams with one  $c_3$  vertex. This is mainly visible in the  $D$  and  $F$  waves, while the  $G$  waves and higher are dominated by OPE. By using a sharp cutoff procedure with  $\Lambda = 500\text{--}800$  MeV, the problematic short-range attraction can be reduced [32], leaving a central potential that is comparable to the one in OBE models. We want to study here if the relativistic amplitudes also result in a short-range central attraction that is weaker.

We present the results for  $D$  and higher waves for the models described in the previous sections. The finite part of the loop integrals has been extracted via both dimensional (using the minimal subtraction scheme in which only the divergent part is removed) and cutoff regularization. For the latter case, a dipole form factor has been chosen and the value of the cutoff  $\Lambda$  has been varied between 663 and 785 MeV, corresponding to  $\Lambda^2 = 0.5\text{--}0.7$  M<sup>2</sup>. With such values for the cutoff, contributions of ranges shorter than about 0.5 fm are effectively cut out. A drawback of a dipole form factor compared with a sharp cutoff is that if a low value for the cutoff  $\Lambda$  is chosen the long-range parts of the potential are distorted to some extent. The choice for a dipole form factor was, however, necessary because of the particular way in which the relativistic diagrams are evaluated and because of the necessary compatibility with the OBE, to which the TPE interaction will be added to determine the lower partial waves.

To extract phase shifts, the OPE contribution has to be added to the one-loop TPE diagrams. For the results presented in this section, the pointlike form of OPE has been used, since multiplying OPE with a form factor would modify even its long-range part by 5–10% when the value of the cutoff is

chosen as low as for the TPE contributions. To determine the phase shifts, the matrix elements of the pseudopotential  $W$  have been used, rather than the iterated  $T$  matrix. In the Born approximation, the scattering amplitude is real. The phase shifts were extracted from the unitary representation of the partial-wave amplitudes,

$$\begin{aligned} T_J^J &= \frac{1}{2ik} [\exp(2i\delta_J) - 1], \\ T_{J\pm 1}^J &= \frac{1}{2ik} [\cos(2\epsilon_J) \exp(2i\delta_{J\pm 1}) - 1], \\ T_{J,J\pm 1}^J &= \frac{1}{2k} \sin(2\epsilon_J) \exp(i\delta_{J-1} + i\delta_{J+1}), \end{aligned} \quad (38)$$

by first computing  $\tan\delta$  in order to avoid problems with inverse trigonometric functions. The difference with simply using  $T_J^J = \delta_J/k$  to extract the phase shifts [17] is at most  $0.5^\circ$  for the cases presented in this section.

We start with the  $D$  waves, plotted in Fig. 8. OPE gives a reasonable result only for the  $^3D_1$  wave, and to some extent to the  $^3D_2$  wave. For the other waves, the agreement is only qualitative. For  $^1D_2$  and  $\epsilon_2$ , the sign is correctly reproduced, but OPE is too weak and too strong, respectively. In the case of the  $^3D_3$  partial wave, even the sign is incorrect. Adding the leading TPE contributions changes the OPE result by at most a few degrees at  $T_{\text{lab}} = 300$  MeV, both for the cutoff (CR) and dimensional regularization (DR) methods. The largest contributions are made by the direct ( $^3D_2$ ,  $^3D_1$ , and  $^3D_3$ ) and crossed ( $^1D_2$  and  $\epsilon_2$ ) boxes. The contributions of the diagrams with the WT vertex are in general small, except in the  $^3D_1$  channel, where their repulsion decreases the phase shift with about  $2^\circ$  at 300 MeV. For the  $^3D_2$  and  $^3D_3$  partial waves, these contributions are even in the wrong direction, most notably for the latter wave.

At NNLO a clear distinction has to be made between the CR and DR results. The former gives a notable improvement in all the partial waves, except  $^3D_1$  and perhaps  $^3D_2$  for which the change is not large enough. The empirical values for the  $^1D_2$  phase shift fall now within the band obtained by varying  $\Lambda$  between 663 and 785 MeV, while the  $^3D_3$  phase shifts have greatly improved. It is noteworthy that an improvement of  $^3D_2$  and  $^3D_3$  would require a higher cutoff. The diagram with the  $c_1$  vertex gives a rather weak isoscalar central attraction, which has only a marginal impact on the  $D$  waves. Similarly, the  $c_2$  term which contributes to the isoscalar central part of the interaction is rather small. Much more important contributions to these waves arise from the diagrams with the  $c_3$  and  $c_4$  vertices, which contribute especially to the isoscalar central and isovector tensor potentials, respectively. The  $c_4$  attractive tensor force is responsible for most of the discrepancy in the  $^3D_1$  channel; while for  $\epsilon_2$ , the  $c_3$  and  $c_4$  contributions have opposite signs and largely compensate each other, leading to an insufficient change toward the experimental values of the phase shifts. The improvements in the  $^1D_2$  and  $^3D_3$  partial waves are due to the attraction resulting from the  $c_3$  term. These statements about the various partial waves are illustrated in Table I, which presents a quantitative comparison of the contributions of the individual diagrams. The phase shifts have been extracted from the amplitude containing contributions

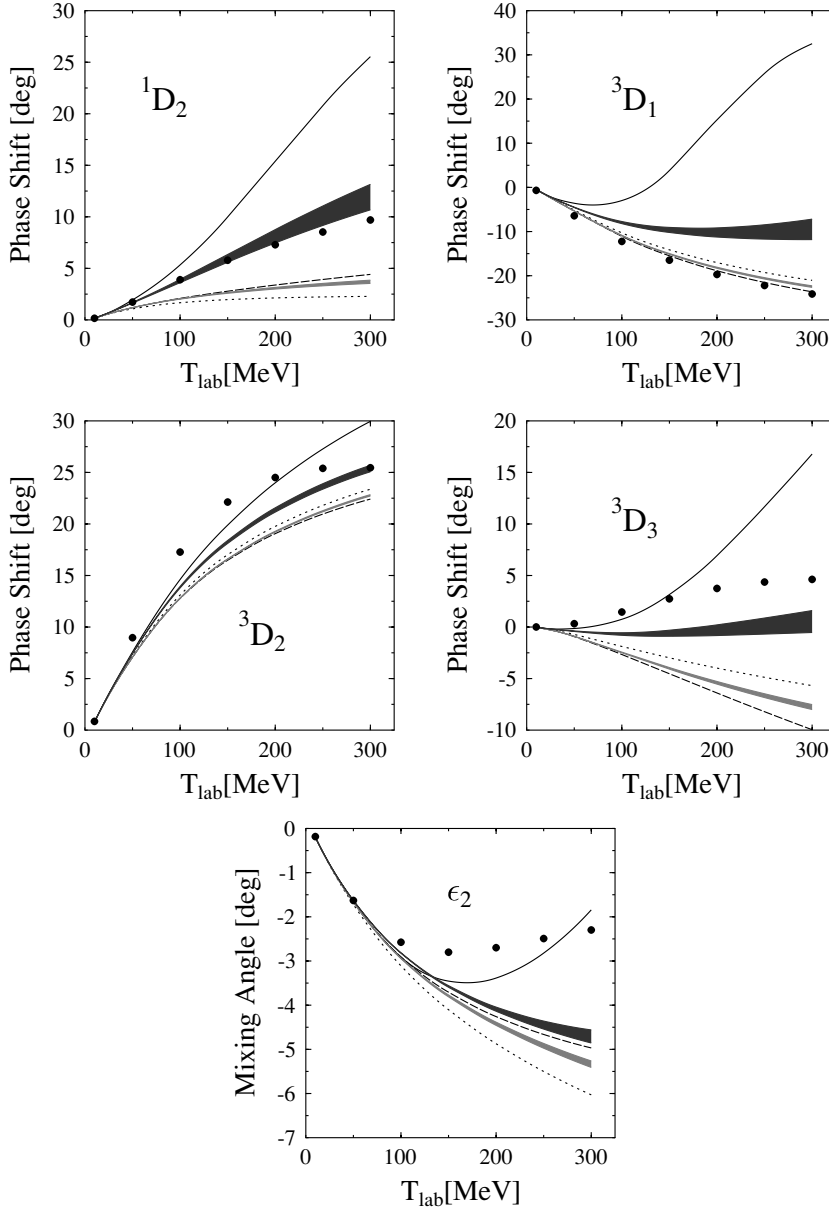


FIG. 8.  $D$ -wave phase shifts and the mixing angle  $\epsilon_2$  as a function of the nucleon kinetic energy in the laboratory frame. Dotted curves represent the pointlike OPE result; dashed and full curves are the dimensional regularization results at NLO and NNLO, respectively. Grey and dark-grey bands correspond to a cutoff regularization calculation at NLO and NNLO, respectively, with the cutoff value varied between 663 and 785 MeV, for a dipole form factor. Phase shifts from energy-dependent partial-wave analysis PWA93 [42] are shown for comparison as bullets.

of the diagram labeling the respective column plus all the diagrams of the columns to the left. By comparing the values in two neighboring columns, one can deduce the relative importance of each of the diagrams at  $T_{\text{lab}} = 200$  MeV, for a value of the cutoff parameter  $\Lambda = 785$  MeV.

Turning to the DR results, the first observation to be made is that the various contributions are far more attractive at higher energies than their CR counterparts. This statement holds for all the  $D$  waves. In the case of  ${}^3D_2$  and  $\epsilon_2$ , this larger attraction leads to a better agreement with the experimental phase shifts at high energies. Our DR results are qualitatively similar to previous results [17,32], but in detail the differences are significant. In Refs. [17,32] the attraction is so strong that the phase shifts reach  $40^\circ$  already at 200 MeV for most of the  $D$  waves. Our CR result is rather similar to that in Ref. [32], the differences originating in the extra terms that we include

(relativistic and recoil corrections) and to the different cutoff scheme.

Next, we discuss the  $F$  waves, cf. Fig. 9. The DR case does not show the strong attraction at the higher energies as was seen for the  $D$  waves. The results of Refs. [17,32] show at these energies an attraction for the  ${}^3F_2$ ,  ${}^3F_3$ , and  ${}^3F_4$  that overshoots our results by  $2^\circ$ – $3^\circ$ . The DR result for the  ${}^1F_3$  wave is close to OPE because of an almost perfect cancellation between the NLO and NNLO TPE diagrams. OPE is a good approximation for all  $F$  waves up to an energy of, at least, 100 MeV. The NLO TPE diagrams are insignificant up to 200 MeV, and they contribute at most half a degree at 300 MeV. The diagram with the  $c_3$  vertex generates a strong attraction in all  $F$  waves, which is compensated to some extent in the  ${}^1F_3$  and  ${}^3F_4$  channels by the isovector tensor repulsion originating in the  $c_4$  diagrams. The mixing angle  $\epsilon_3$  decreases with respect

TABLE I. Contributions of the individual TPE diagrams at  $T_{\text{lab}} = 200$  MeV with the cut-off  $\Lambda = 785$  MeV and pointlike OPE. The result in each column is obtained by adding the tabulated contribution to the one in the left-neighboring column. These additions were done at the level of the scattering amplitudes and only then phase shifts were extracted. DB stands for the irreducible part of the direct box,  $c_0c_4$  for the football diagram with one WT and one  $c_4$  vertex, *etc.*

	OPE	+DB	+CB	+ $c_0$	+ $c_1$	+ $c_2$	+ $c_3$	+ $c_4$	+ $c_0c_4$
$^3D_1$	-17.03	-19.33	-19.26	-18.32	-18.17	-17.50	-14.99	-9.99	-9.17
$^1D_2$	2.13	2.11	3.27	3.15	3.41	3.78	7.87	8.72	8.76
$^3D_2$	19.76	19.10	18.79	19.21	19.36	19.76	21.98	21.47	21.57
$^3F_2$	1.87	1.78	1.75	1.66	1.71	1.85	2.52	2.17	2.13
$\epsilon_2$	-4.87	-4.78	-4.44	-4.38	-4.40	-4.37	-4.85	-4.09	-4.04
$^1F_3$	-3.52	-3.56	-3.71	-3.64	-3.58	-3.52	-2.74	-3.26	-3.27
$^3F_3$	-3.21	-3.24	-3.07	-3.11	-3.05	-2.96	-2.21	-2.17	-2.18
$^3D_3$	3.98	-5.52	-5.82	-5.54	-5.26	-5.45	-0.70	0.30	0.21
$^3G_3$	-2.12	-2.29	-2.28	-2.23	-2.22	-2.19	-2.05	-1.86	-1.84
$\epsilon_3$	6.44	6.63	6.59	6.56	6.56	6.56	6.51	6.19	6.17
$^1G_4$	0.67	0.67	0.73	0.73	0.74	0.76	0.92	0.95	0.95
$^3G_4$	4.54	4.47	4.45	4.48	4.49	4.51	4.66	4.64	4.65
$^3F_4$	0.55	0.51	0.64	0.62	0.69	0.66	1.55	1.50	1.50
$^3H_4$	0.31	0.30	0.30	0.30	0.30	0.30	0.34	0.33	0.33
$\epsilon_4$	-1.09	-1.09	-1.07	-1.07	-1.07	-1.07	-1.07	-1.05	-1.04
$^3G_5$	-0.75	-0.84	-0.86	-0.85	-0.83	-0.83	-0.65	-0.62	-0.62

to its NLO value by about  $1^\circ$  at 300 MeV because of the  $c_4$  repulsion. The cutoff dependence of the  $F$  waves at the higher energies is much less than for the  $D$  waves and especially small for the  $^1F_3$  and  $^3F_2$  waves. Except for  $^3F_2$ , all the  $F$  phase shifts and  $\epsilon_3$  are in rather good agreement with PWA93.

The phase shifts of the  $G$  waves and the mixing angle  $\epsilon_4$  are plotted in Fig. 10. The difference between the DR and CR has reduced even further, compared to the  $F$  waves. As expected, OPE is the major contributor, while the effect of the NLO diagrams is small, about  $0.2^\circ$  at 300 MeV. NNLO diagrams that have a significant impact on the  $G$  waves are once more the triangle ones with the  $c_3$  and  $c_4$  coupling constants. The value of the  $\epsilon_4$  mixing angle is well reproduced by OPE. When comparing with the empirical phase shifts, significant differences are observed in the  $^3G_3$  and  $^3G_5$  waves. We will come back to this below. The  $H$  and  $I$  waves, finally, are to a high degree determined by OPE. There is only one exception, the  $^3H_6$  wave, which receives an attractive contribution from the  $c_3$  triangle diagram that increases the value of its phase shift by some 60%.

In the plots, we have compared calculations with dimensional and cutoff regularization. To study the effect of a low cutoff on the short range of the potential, one should really compare such a calculation with the one obtained by letting the cutoff  $\Lambda$  grow to infinity. We have performed such a calculation and present the cutoff sensitivity of the various waves in Table II. To demonstrate the sensitivity, the results for the phase shifts at  $T_{\text{lab}} = 200$  MeV are shown for three values of the cutoff:  $\Lambda^2 = 1.67, 1.01, \text{ and } 0.62$  GeV $^2$ . The last value corresponds to the lower limits of the cutoff bands in the plots, while the first value is rather high such that it approaches a pointlike ( $\Lambda \rightarrow \infty$ ) interaction. Two features are readily seen: sensitivity is higher toward lower values of the cutoff (according to expectations), and the main part of

the cutoff sensitivity originates in the NNLO diagrams. The  $\Lambda \rightarrow \infty$  and the DR calculations are, without renormalization, not identical, but they will differ by a polynomial term, that is,

$$\begin{aligned}
 W_{\text{DR}} &= W_{\text{DR}}^{(\text{non-pol.})} + W_{\text{DR}}^{(\text{pol.})}, \\
 W_{\text{CR}} &= W_{\text{CR}}^{(\text{non-pol.})} + W_{\text{CR}}^{(\text{pol.})}, \\
 W_{\text{CR}}^{(\text{non-pol.})} &\xrightarrow{\Lambda \rightarrow \infty} W_{\text{DR}}^{(\text{non-pol.})}.
 \end{aligned}
 \tag{39}$$

The two polynomials have a similar structure, with the cutoff mass  $\Lambda$  and the renormalization scale  $\mu$  interchanged and with different coefficients for the monomials. The difference between the two results from short-range contact potentials. The difference between the  $\Lambda^2 = 1.67$  GeV $^2$  and the DR calculations is sizable for the  $D$  waves, which are sensitive to contact potentials with four derivatives or more. It amounts up to half of the observed difference between the DR and low cutoff calculations ( $^3D_1$  and  $^3D_3$ ). The difference is small for the  $F$  waves, with the exception of the  $^3F_2$  wave.

## B. Iteration of the potential

In the previous section, the phase shifts were computed in a Born approximation. For a number of partial waves ( $^3D_1, ^3D_2, ^3D_3, ^3F_2, \text{ and } ^3G_5$ ) significant differences with respect to PWA93 were observed, some of the phase shifts being numerically small. We have, therefore, iterated the BSLT equation and extracted the resulting phase shifts in order to see if this helps to improve the situation. Some of the phase shifts are plotted in Fig. 11. In contrast with the procedure of the previous section, now also OPE is regularized by a dipole form factor, with the value of the cutoff parameter chosen to be the same as the one used in computing the one-loop TPE diagrams. Adding such a form factor for OPE changes

TABLE II. Cut-off dependence of the peripheral phase-shifts at  $T_{\text{lab}} = 200$  MeV. For comparison also the pointlike OPE result for each of the considered partial waves is shown. Three values were chosen for the cutoff parameter that regularize the one-loop TPE contributions: the largest,  $\Lambda = 1.293$  GeV, corresponds to an almost pointlike interaction, while the lowest,  $\Lambda = 0.785$  GeV, was one of the “low values” used to produce the results of this section; cf. Fig. 8. Separate results at NLO and NNLO are presented.

$\Lambda(\text{GeV})$	OPE D.R.	NLO			NNLO		
		1.293	1.006	0.785	1.293	1.006	0.785
${}^3D_1$	-17.03	-18.70	-18.57	-18.32	-2.15	-5.72	-9.17
${}^1D_2$	2.13	3.42	3.32	3.15	11.64	10.42	8.76
${}^3D_2$	19.76	19.04	19.11	19.21	22.43	22.09	21.57
${}^3F_2$	1.87	1.63	1.64	1.66	2.02	2.08	2.13
$\epsilon_2$	-4.87	-4.25	-4.30	-4.38	-3.86	-3.95	-4.04
${}^1F_3$	-3.52	-3.65	-3.65	-3.64	-3.27	-3.27	-3.27
${}^3F_3$	-3.21	-3.12	-3.12	-3.11	-2.11	-2.12	-2.18
${}^3D_3$	-3.98	-6.09	-5.86	-5.54	3.14	1.75	0.21
${}^3G_3$	-2.12	-2.23	-2.23	-2.23	-1.84	-1.84	-1.84
$\epsilon_3$	6.44	6.58	6.57	6.56	6.12	6.14	6.17
${}^1G_4$	0.67	0.72	0.73	0.73	0.95	0.95	0.95
${}^3G_4$	4.54	4.48	4.48	4.48	4.65	4.65	4.65
${}^3F_4$	0.55	0.62	0.62	0.62	1.65	1.60	1.50
${}^3H_4$	0.31	0.30	0.30	0.30	0.32	0.32	0.33
$\epsilon_4$	-1.09	-1.07	-1.07	-1.07	-1.05	-1.04	-1.04
${}^3G_5$	-0.75	-0.85	-0.85	-0.85	-0.62	-0.62	-0.62

somewhat the phase shifts compared to the Born result, most notably for the  ${}^3D_2$  and  ${}^3F_3$  waves. To see this, one should compare the light-grey bands in Fig. 11 with the NNLO results plotted in the previous section (Figs. 8–10).

Besides the effect of the iteration, the effect of adding only the once-iterated OPE term to the quasipotential has also been plotted. We find that this can have an important impact on the value of the phase shifts of certain waves. It results in an improvement of all phase shifts for which the Born approximation showed a significant difference compared with PWA93. Three such examples are plotted in Fig. 11, where one should compare the light-grey and the grey bands. Not shown is the  ${}^3D_1$  partial wave for which the iteration of OPE leads to a dramatic change in the value of the phase shift, decreasing it by  $20^\circ$  at 300 MeV. Iterating the potential increases its value to  $-13^\circ$  at 300 MeV, which is only marginally better than the result of Fig. 8. Other waves for which the result improves by solving the quasipotential equation are  ${}^3D_3$ ,  ${}^3G_3$ ,  ${}^3G_5$ , and  ${}^3D_2$ .

In general, for these waves, one observes that adding the once-iterated OPE potential already produces an significant shift toward PWA93, subsequent iterations of OPE and TPE having only a small effect. The  ${}^3F_3$  partial wave is not affected noticeably by the iteration. For  ${}^3F_2$ , another problematic wave, the change is in the good direction, but it is only marginal. This is the only wave (together with the  $\epsilon_2$  mixing angle) that still shows a sizable disagreement from the data. This is likely because it is coupled to the  ${}^3P_2$  wave, for which the short-range interaction is important.

Up to now, we have used fixed values for the chiral coupling constants:  $c_1 = -0.81$ ,  $c_2 = 3.28$ ,  $c_3 = -4.70$ , and

$c_4 = 3.40$ , expressed in  $\text{GeV}^{-1}$ , which are consistent with the range of values found from  $\pi N$  amplitudes [27,28] and in fits to  $NN$  scattering data [19,20]. It is interesting to investigate how sensitive the description of the peripheral phase shifts is to variations in these coupling constants. Since the contribution of the diagrams proportional to the  $c_1$  and  $c_2$  coupling constants is small, we will keep their values fixed to  $c_1 = -0.81$  and  $c_2 = 3.28$ , respectively. We vary the values of  $c_3$  and  $c_4$  by hand within the range  $c_3 = -2.0$  to  $-6.0$  and  $c_4 = 3.0$  to  $6.5$ , and we study the resulting description of the  $D$ ,  $F$ , and  $G$  waves. The value of the cutoff will be varied as before in the range  $\Lambda^2 = 0.5\text{--}0.7 M^2$ .

In Fig. 12, we present the results for selected peripheral partial waves for three sets of values of the coupling constants: (I)  $c_1 = -0.81$ ,  $c_2 = 3.28$ ,  $c_3 = -4.70$ ,  $c_4 = 3.40$ ; (II)  $c_1 = -0.81$ ,  $c_2 = 3.28$ ,  $c_3 = -3.90$ ,  $c_4 = 4.50$ ; and (III)  $c_1 = -0.81$ ,  $c_2 = 3.28$ ,  $c_3 = -3.30$ ,  $c_4 = 5.30$ . The results are depicted by the light-grey, grey, and dark-grey bands, respectively. The last two sets give a better description of the  $D$ ,  $F$ , and  $G$  waves at laboratory energies higher than 200 MeV than does the original set (I). The only exception is the  ${}^3D_1$  partial wave, while for  ${}^3F_2$  and  $\epsilon_2$  the description is still deficient. For these channels, short-range contributions should be important. This procedure leads us to estimate that for the best description of the peripheral waves, the following ranges for the coupling constants are favored by our model:  $c_3 = -4.0 \pm 1.0$  and  $c_4 = +4.5 \pm 1.0$ .

A comparison between the description of the peripheral phase shifts of our model and the description of them in Refs. [16,43] reveals differences mainly in the  $D$  waves. This is understandable, since chiral models include contact terms

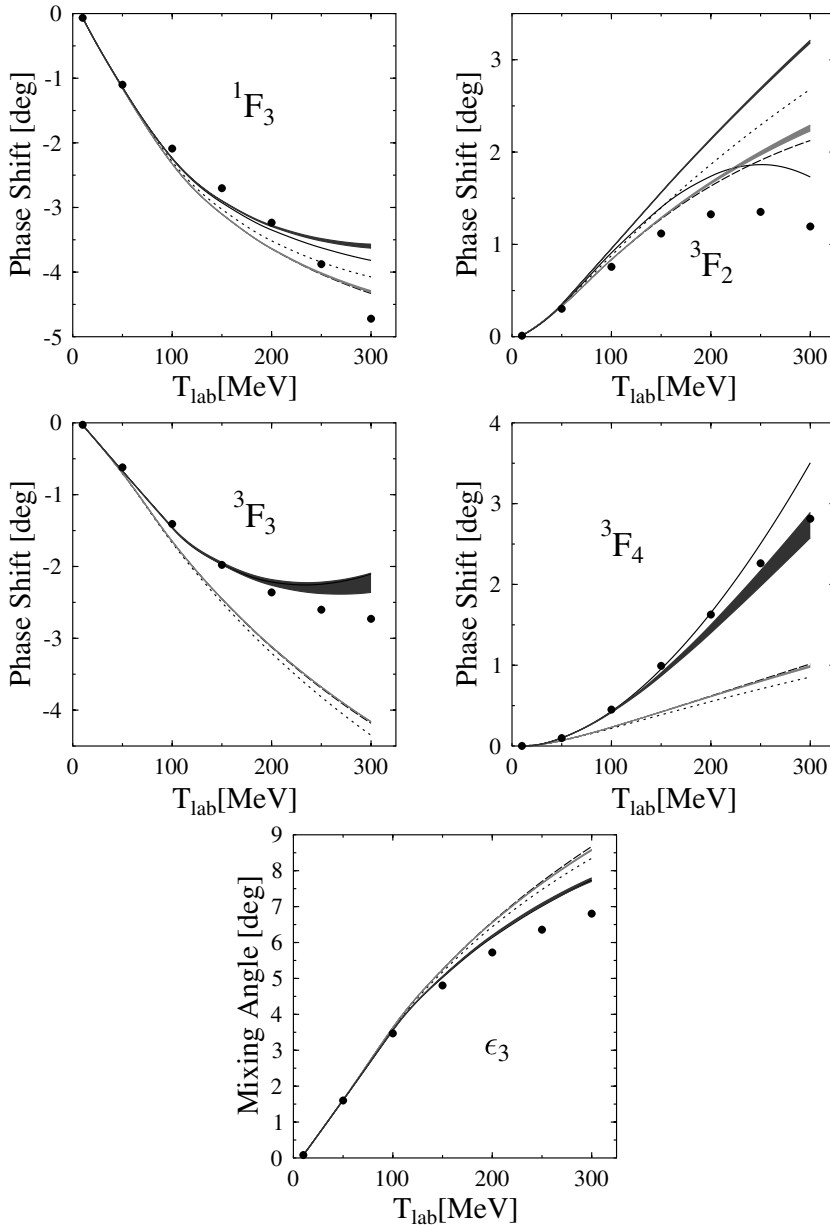


FIG. 9. Same as in Fig. 8, but for  $F$  waves and  $\epsilon_3$  mixing angle.

that can be fitted for each of these partial waves individually. We expect that the shortcomings in our description of the  $^3D_1$  phase shift and  $\epsilon_2$  mixing angle can be cured when short-range contributions are included. Our model describes well the  $^3D_3$  partial wave, while the quality of the description of the  $F$  and  $G$  phase shifts in our model and those in Refs. [16,43] are similar. Some of these partial waves show deviations from the experimental data above 200 MeV:  $^3F_2$ ,  $^3F_3$ , and  $^3G_5$ , the deviations being of comparable magnitude.

### C. Numerical accuracy of the results

In our calculation, numerical inaccuracies can originate from two sources: First, the finite accuracy with which the scalar loop integrals are computed by using the  $ff$  libraries, and second, the method for treating the cutoff integrals. Of

course, in the case of DR, only the first source is relevant. The  $ff$  libraries [38] have been developed for the evaluation of scalar loop integrals that are encountered in particle physics. They are based on more developed numerical algorithms than the predecessor FORMF [34] written by Veltman to perform the same task. The  $ff$  comes with built-in error evaluation routines. Unfortunately, these routines proved unreliable in our case, and in order to determine the numerical accuracy we have resorted to an explicit comparison between the outputs of  $ff$  and FORMF. This has been done for a few relevant kinematic cases characteristic of our particular model. In all cases, the outputs of the two programs were identical up to eight digits or more.

The second source of inaccuracy has proved to be the more serious one. Each meson propagator is multiplied with a dipole form factor. Since the  $ff$  program can only handle four-point functions or lower, the following reduction has to be applied:

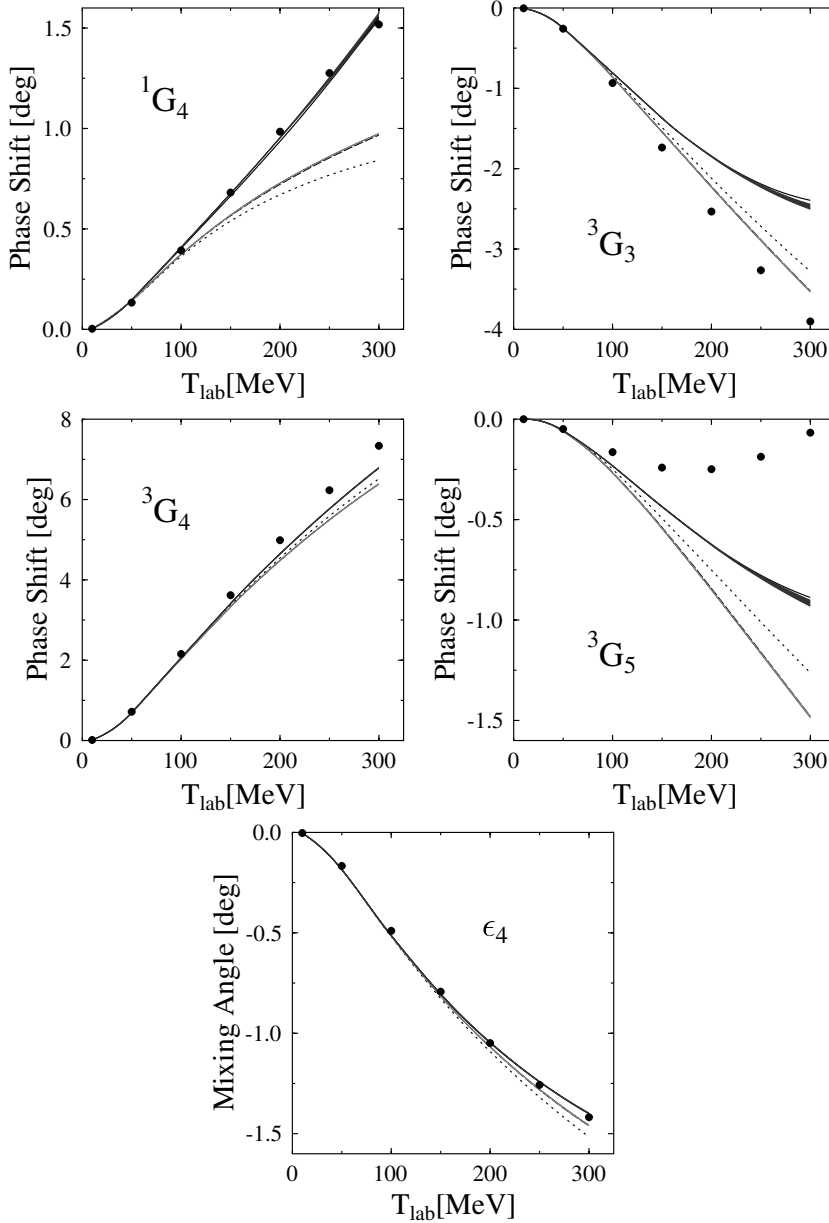


FIG. 10. The  $G$  waves and the  $\epsilon_4$  mixing angle. The curves have the same meaning as in Fig. 8.

$$\begin{aligned}
 \frac{1}{k^2 - m_\pi^2} \left[ \frac{\Lambda^2}{k^2 - \Lambda^2} \right]^2 &\simeq \frac{1}{k^2 - m_\pi^2} \frac{\Lambda^2}{k^2 - (\Lambda^2 - \varepsilon)} \frac{\Lambda^2}{k^2 - (\Lambda^2 + \varepsilon)} \\
 &= \frac{\Lambda^4}{\Lambda^2 - m_\pi^2} \left[ \frac{1}{2\varepsilon} \left( \frac{1}{k^2 - (\Lambda^2 + \varepsilon)} - \frac{1}{k^2 - (\Lambda^2 - \varepsilon)} \right) - \frac{1}{\Lambda^2 - m_\pi^2} \left( \frac{1}{k^2 - \Lambda^2} - \frac{1}{k^2 - m_\pi^2} \right) \right]. \quad (40)
 \end{aligned}$$

The approximation in the first line becomes an identity when  $\varepsilon$  approaches zero. As can be seen from the second line, this limit result in severe cancellations which can lead to a significant loss of accuracy. Very small values of  $\varepsilon$  are thus counterproductive, but so are larger values, since in that case the approximation in the first line becomes poor. By varying

$\varepsilon$  from very small to larger for a specific range of values, a plateau can be reached where the accuracy is maximal. In the actual calculations, the value  $\varepsilon = 0.044 \text{ GeV}^2$  has been used. This value is toward the right edge of the maximum accuracy plateau and leads to a reasonable accuracy for all the cases of interest here. To show the sensitivity of our results with

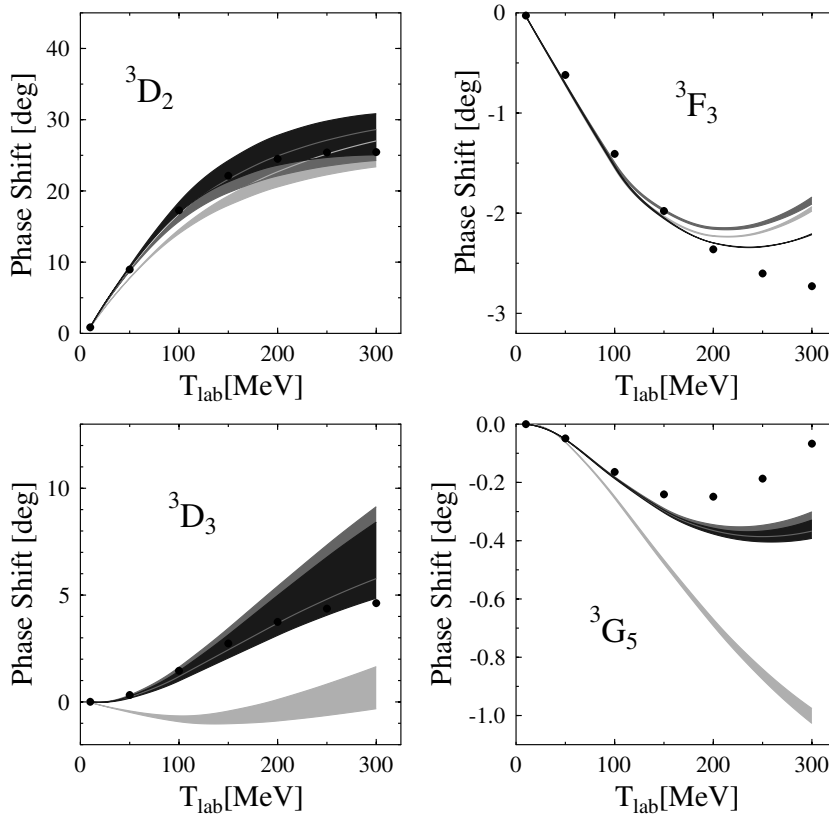


FIG. 11. Selected waves for which the effect of the iteration of the quasipotential  $W$  is shown (dark-grey band). Born result is represented by the light-grey band. Effect of adding the once-iterated OPE term to  $W$  is also shown (grey band).

respect to this parameter, we varied it in the range from 0.022 to 0.066  $\text{GeV}^2$ . In Fig. 13, the difference between these two extreme cases and the case with  $\varepsilon = 0.044 \text{ GeV}^2$  is plotted for two representative phase shifts, for both the NLO and the full results. The difference grows with energy (similar to the cutoff sensitivity) and is greatest for the  $D$  waves (up to  $0.1^\circ$ ). It is much smaller for  $F$  and is practically zero for higher waves. Changing the range variation for  $\varepsilon$  to 0.009–0.088  $\text{GeV}^2$ , the difference shows an important increase, indicating that the maximum accuracy plateau has been left.

## V. SUMMARY AND CONCLUSIONS

In this paper, we have considered the extension of the kernel of the relativistic OBE model for elastic  $NN$  scattering by adding the counterparts of the one-loop TPE diagrams that contribute at NLO and NNLO in nonrelativistic chiral EFT. This means that in addition we include relativistic and recoil correction terms. The method that we use to evaluate the one-loop diagrams has allowed an easy implementation of both dimensional and dipole cutoff regularization. The BSLT equation could only be solved in the CR scheme because of the need for a second cutoff in the quasipotential equation, which, for consistency, had to be of the same type as the one regularizing the potential. We have studied in this paper only the “peripheral” ( $D$ ,  $F$ ,  $G$ ) waves, since in this way the model dependence introduced by short-range physics, which would mean exchanges of heavy mesons in our case, could be

avoided. Thus, the validity of using only OPE and chiral TPE for these waves was tested.

The contributions from the diagrams with a  $c_3$  and  $c_4$  vertex are strong. They incorporate physics attributed to the  $\Delta$  isobar. The  $c_3$  diagram is the origin of a strong medium-range isoscalar-scalar attraction. This is clearly visible in the  $D$  waves computed via DR. Compared to the corresponding nonrelativistic results [17,32], the scalar attraction that we observe is less pronounced, but still too strong to allow a reproduction of the  $D$ -wave phase shifts above 100 MeV. The relatively smaller central attraction in our case is due to the relativistic and recoil corrections that are included in our framework. The DR results for most  $F$  and higher partial waves are reasonably close to the experimental values.

In order to suppress the strong isoscalar-central attraction for the DR results for the  $D$  waves, we have alternatively made use of a CR scheme with a dipole form factor to regularize the one-loop TPE diagrams. The cutoff value  $\Lambda$  has been varied in order to reproduce the  $D$  waves as closely as possible. Values of  $\Lambda$  in the band 663–785 MeV give good qualitative results. Within the same range for the cutoff, an improvement for some of the  $F$  waves with respect to the DR result is also observed. Compared with the nonrelativistic case [32], we obtain a similar good description of the peripheral waves with a somewhat higher value for the cutoff parameter regularizing the one-loop diagrams: one should compare  $\Lambda = 650\text{--}800 \text{ MeV}$  within our model with  $\Lambda = 500\text{--}800 \text{ MeV}$  in the nonrelativistic treatment. The results for the phase shifts are very sensitive to the cutoff value at energies close to the pion-production threshold, most of the sensitivity originating

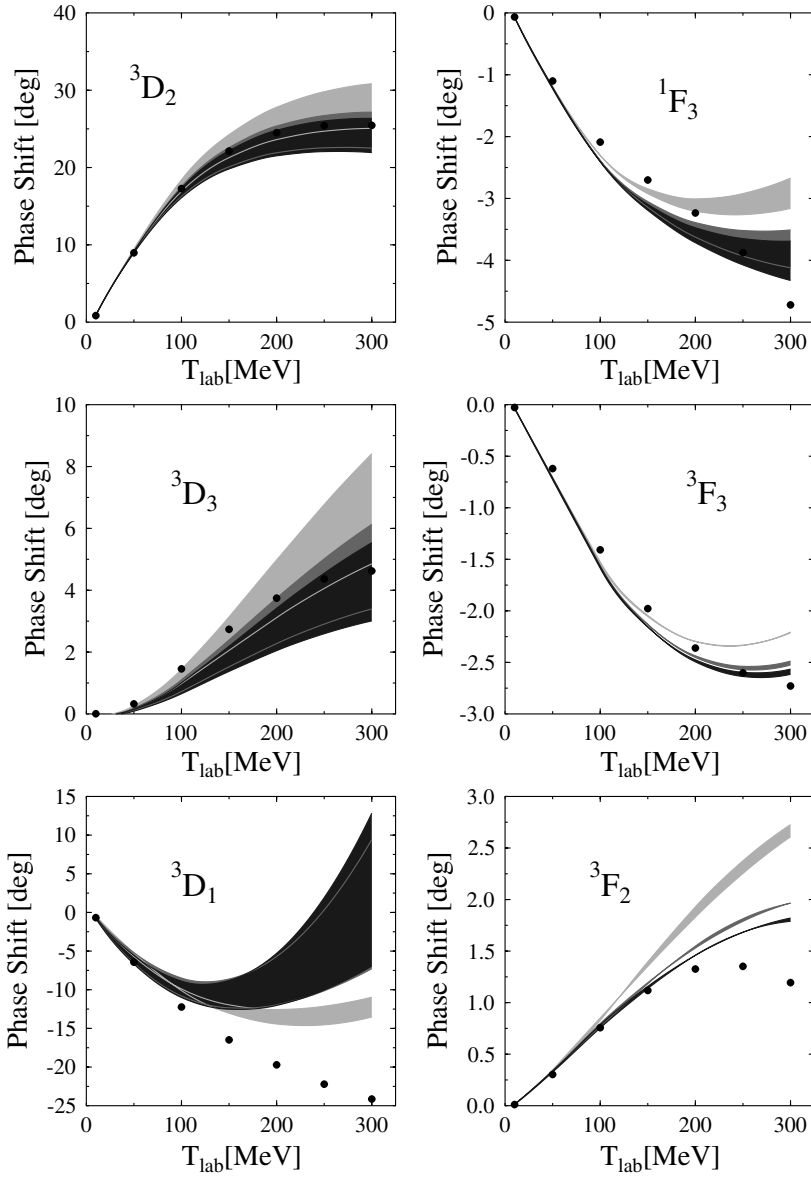


FIG. 12. Sensitivity of selected phase shifts with respect to variation of the coupling constants  $c_3$  and  $c_4$ . Light-grey, grey and dark-grey bands correspond to the sets of values for the LECs denoted in the text by (I), (II), and (III) respectively.

from the NNLO contributions. Solving the BSLT equation for the peripheral waves results in an improvement of the problematic  ${}^3D_3$ ,  ${}^3D_2$ , and  ${}^3G_5$  partial waves. For other waves, such as  ${}^3D_1$  and  ${}^3F_2$ , the improvement is only marginal because

of their sensitivity to the short-range interaction. We varied the values of the  $c_3$  and  $c_4$  couplings and extracted a range for their values that is favored by our model:  $c_3 = -4.0 \pm 1.0 \text{ GeV}^{-1}$  and  $c_4 = +4.5 \pm 1.0 \text{ GeV}^{-1}$ .

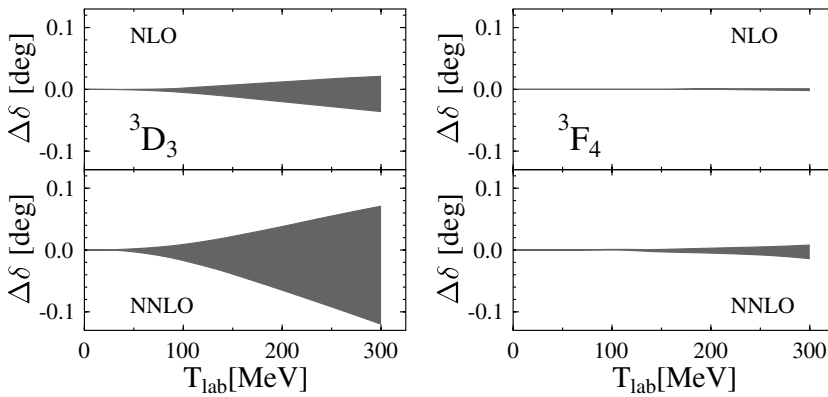


FIG. 13. Sensitivity of phase shifts to variation of  $\epsilon$  parameter. NLO and NNLO results are shown separately.

As a final conclusion, an OPE model that includes chiral TPE allows a reasonable description to be made of the peripheral waves in  $NN$  scattering within a relativistic framework, once the short-range isoscalar-scalar attraction is dampened by a low-value cutoff. In a future publication, we will take the next step to address the low partial waves, taking into account also the short-range interactions.

### APPENDIX: SCALAR MOMENTS

In this Appendix, we will summarize the strategy used to express the tensor integrals in Eq. (31) in terms of scalar moments. The procedure is simple: one has to meet in the final answer all tensor quantities of the same rank as the starting tensor integral. We start with the two-point functions, for which one has

$$B_\mu(p, m_1, m_2) = p_\mu B_{11}, \quad (A1)$$

$$B_{\mu\nu}(p, m_1, m_2) = p_\mu p_\nu B_{21} + g_{\mu\nu} B_{22}.$$

For the two-point functions, analytical expressions can be obtained [34,35]. The calculations in this work require  $C$  moments up to the third rank, viz.,

$$C_\mu = p_\mu C_{11} + q_\mu C_{12},$$

$$C_{\mu\nu} = p_\mu p_\nu C_{21} + q_\mu q_\nu C_{22} + \{p, q\}_{\mu\nu} C_{23} + g_{\mu\nu} C_{24},$$

$$C_{\mu\nu\rho} = p_\mu p_\nu p_\rho C_{31} + q_\mu q_\nu q_\rho C_{32} + \{ppq\}_{\mu\nu\rho} C_{33} \\ + \{pqq\}_{\mu\nu\rho} C_{34} + \{pg\}_{\mu\nu\rho} C_{35} + \{qg\}_{\mu\nu\rho} C_{36},$$

$$\{pq\}_{\mu\nu} = p_\mu q_\nu + p_\nu q_\mu, \\ \{ppq\}_{\mu\nu\rho} = p_\mu p_\nu q_\rho + p_\mu p_\rho q_\nu + p_\rho p_\nu q_\mu, \\ \{pg\}_{\mu\nu\rho} = p_\mu g_{\nu\rho} + p_\nu g_{\mu\rho} + p_\rho g_{\mu\nu}. \quad (A2)$$

For the  $D$  tensor integrals, one writes the following decomposition (again only up to the third rank):

$$D_\mu = p_\mu D_{11} + q_\mu D_{12} + r_\mu D_{13},$$

$$D_{\mu\nu} = p_\mu p_\nu D_{21} + q_\mu q_\nu D_{22} + r_\mu r_\nu D_{23} + \{pq\}_{\mu\nu} D_{24} \\ + \{pr\}_{\mu\nu} D_{25} + \{qr\}_{\mu\nu} D_{26} + g_{\mu\nu} D_{27},$$

$$D_{\mu\nu\rho} = p_\mu p_\nu p_\rho D_{31} + q_\mu q_\nu q_\rho D_{32} + r_\mu r_\nu r_\rho D_{33} \\ + \{ppq\}_{\mu\nu\rho} D_{34} + \{ppr\}_{\mu\nu\rho} D_{35} + \{pqq\}_{\mu\nu\rho} D_{36} \\ + \{prr\}_{\mu\nu\rho} D_{37} + \{qqr\}_{\mu\nu\rho} D_{38} + \{qrr\}_{\mu\nu\rho} D_{39} \\ + \{pqr\}_{\mu\nu\rho} D_{310} + \{pg\}_{\mu\nu\rho} D_{311} + \{qg\}_{\mu\nu\rho} D_{312} \\ + \{rg\}_{\mu\nu\rho} D_{313},$$

$$\{pqr\}_{\mu\nu\rho} = p_\mu \{qr\}_{\nu\rho} + p_\nu \{qr\}_{\mu\rho} + p_\rho \{qr\}_{\mu\nu}. \quad (A3)$$

The kinematic conventions for the two-, three-, and four-point functions are the ones displayed in Fig. 7. The three- and four-point scalar moments cannot be expressed in a closed form. For the  $C_0$  and  $D_0$  moments, formulas in terms of Spence functions can be derived for certain kinematic situations [35]. The values of the higher scalar moments can be found once the values of the zero-order moments are known. A simple method to achieve this is presented in Ref. [34]. To avoid kinematic singularities, the calculation of scalar moments in the  $ff$  package is implemented using different, more refined algorithms [38,39].

- 
- [1] M. M. Nagels, T. A. Rijken, and J. J. de Swart, Phys. Rev. D **17**, 768 (1978); V. G. J. Stoks, R. A. M. Klomp, C. P. F. Terheggen, and J. J. de Swart, Phys. Rev. C **49**, 2950 (1994).
- [2] R. Timmermans, Th. A. Rijken, and J. J. de Swart, Phys. Rev. C **50**, 48 (1994).
- [3] J. Fleischer and J. A. Tjon, Nucl. Phys. **B84**, 375 (1974); Phys. Rev. D **15**, 2537 (1977); **21**, 87 (1980).
- [4] J. A. Tjon and E. E. van Faassen, Phys. Lett. **B120**, 39 (1983); E. E. van Faassen and J. A. Tjon, Phys. Rev. C **28**, 2354 (1983); **30**, 285 (1986).
- [5] E. Hummel and J. A. Tjon, Phys. Rev. Lett. **63**, 1788 (1989); Phys. Rev. C **42**, 423 (1990); **49**, 21 (1994).
- [6] G. H. Martinus, O. Scholten, and J. A. Tjon, Phys. Rev. C **56**, 2945 (1997); **58**, 686 (1998).
- [7] M. D. Cozma, G. H. Martinus, O. Scholten, R. G. E. Timmermans, and J. A. Tjon, Phys. Rev. C **65**, 024001 (2002); M. D. Cozma, O. Scholten, R. G. E. Timmermans, and J. A. Tjon, *ibid.* **68**, 044003 (2003).
- [8] D. B. Kaplan and A. V. Manohar, Phys. Rev. C **56**, 76 (1997).
- [9] S. Weinberg, Phys. Lett. **B251**, 288 (1990); Nucl. Phys. **B363**, 3 (1991).
- [10] C. Ordóñez and U. van Kolck, Phys. Lett. **B291**, 459 (1992).
- [11] C. Ordóñez, L. Ray, and U. van Kolck, Phys. Rev. Lett. **72**, 1982 (1994); Phys. Rev. C **53**, 2086 (1996).
- [12] D. B. Kaplan, M. J. Savage, and M. B. Wise, Nucl. Phys. **B534**, 329 (1998).
- [13] S. Fleming, T. Mehen, and I. W. Stewart, Nucl. Phys. **A677**, 313 (2000).
- [14] A. Nogga, R. G. E. Timmermans, and U. van Kolck, Phys. Rev. C **72**, 054006 (2005).
- [15] E. Epelbaum, W. Glöckle, and U.-G. Meißner, Nucl. Phys. **A637**, 107 (1998); **A671**, 295 (2000).
- [16] D. R. Entem and R. Machleidt, Phys. Rev. C **66**, 014002 (2002); **68**, 041001(R) (2003).
- [17] N. Kaiser, R. Brockmann, and W. Weise, Nucl. Phys. **A625**, 758 (1997).
- [18] J. L. Friar, Phys. Rev. C **60**, 034002 (1999).
- [19] M. C. M. Rentmeester, R. G. E. Timmermans, J. L. Friar, and J. J. de Swart, Phys. Rev. Lett. **82**, 4992 (1999).
- [20] M. C. M. Rentmeester, R. G. E. Timmermans, and J. J. de Swart, Phys. Rev. C **67**, 044001 (2003).
- [21] V. G. Kadyshevsky, Nucl. Phys. **B6**, 125 (1968); F. Gross, Phys. Rev. **186**, 1448 (1969); R. H. Thompson, Phys. Rev. D **1**, 110 (1970).
- [22] A. A. Logunov and A. N. Tavkhelidze, Nuovo Cimento **29**, 380 (1963); R. Blankenbecler and R. Sugar, Phys. Rev. **142**, 1051 (1966).
- [23] S. Weinberg, *The Quantum Theory of Fields* (Cambridge University Press, Cambridge, United Kingdom, 1996), Vol. 2.
- [24] J. Gasser, M. E. Sainio, and A. Svarc, Nucl. Phys. **B307**, 779 (1988).
- [25] E. Jenkins and A. V. Manohar, Phys. Lett. **B255**, 558 (1991).
- [26] V. Bernard, N. Kaiser, J. Kambor, and U.-G. Meißner, Nucl. Phys. **388**, 315 (1992).

- [27] V. Bernard, N. Kaiser, and U.-G. Meißner, Nucl. Phys. **A615**, 483 (1997); N. Fettes, Ulf-G. Meißner, and S. Steininger, Nucl. Phys. **A640**, 199 (1998).
- [28] P. Büttiker and U.-G. Meißner, Nucl. Phys. **A668**, 97 (2000).
- [29] C. A. da Rocha and M. R. Robilotta, Phys. Rev. C **49**, 1818 (1994).
- [30] W. R. Wortman, Phys. Rev. **176**, 1762 (1968).
- [31] N. Kaiser, Phys. Rev. C **64**, 57001 (2001); **65**, 017001 (2002).
- [32] E. Epelbaum, W. Glöckle, and U.-G. Meißner, Eur. Phys. J. **A19**, 125 (2004).
- [33] V. Stoks, R. Timmermans, and J. J. de Swart, Phys. Rev. C **47**, 512 (1993).
- [34] G. Passarino and M. Veltman, Nucl. Phys. **B160**, 151 (1979).
- [35] G. 't Hooft and M. Veltman, Nucl. Phys. **B153**, 365 (1979).
- [36] M. J. Zuilhof and J. A. Tjon, Phys. Rev. C **26**, 1277 (1982).
- [37] L. S. Celenza, A. Pantziris, and C. M. Shakin, Phys. Rev. C **46**, 2213 (1992).
- [38] G. J. van Oldenborgh and J. A. M. Vermaseren, Z. Phys. C **46**, 425 (1990).
- [39] W. L. van Neerven and J. A. M. Vermaseren, Phys. Lett. **B137**, 241 (1984).
- [40] J. Vermaseren, <http://www.nikhef.nl/form/>.
- [41] J. Kubis, Phys. Rev. D **6**, 547 (1972).
- [42] V. G. J. Stoks, R. A. M. Klomp, M. C. M. Rentmeester, and J. J. de Swart, Phys. Rev. C **48**, 792 (1993); <http://nn-online.org/>.
- [43] E. Epelbaum, W. Glöckle, and U.-G. Meißner, Nucl. Phys. **A747**, 362 (2005); E. Epelbaum, Prog. Part. Nucl. Phys. **57**, 654 (2006).